Morphology and Mixing State of Aged Soot Particles at a Remote Marine Free-tropospheric Site: Implications to Optical Properties

Swarup China[1,2], Barbara Scarnato[3], Robert C. Owen[4], Bo Zhang[1], Marian T. Ampadu[5], Sumit Kumar[1,2], Katja Dzepina[1,5], Michael P. Dziobak[1], Paulo Fialho[6], Judith A. Perlinger[1,7], Jacques Hueber[8], Detlev Helmig[8], Lynn R. Mazzoleni[1,5], and Claudio Mazzoleni[1,2]

[1]Atmospheric Sciences Program, Michigan Technological University, Houghton, MI, USA

[2]Department of Physics, Michigan Technological University, Houghton, MI, USA

[3]Naval Postgraduate School, Monterey, CA, USA

[4]US EPA, Research Triangle Park, NC, USA

[5]Department of Chemistry, Michigan Technological University, Houghton, MI, USA

[6]University of Azores, Angra do Heroísmo, Portugal

[7]Department of Civil and Environmental Engineering, Michigan Technological University, Houghton, MI, USA

[8]Institute of Alpine and Arctic Research, University of Colorado, Boulder, CO, USA

Geophysical Research Letters

Corresponding authors:

Swarup China (schina@mtu.edu) and Claudio Mazzoleni (cmazzoleni@mtu.edu)

Abstract

The radiative properties of soot particles depend on their morphology and mixing state, but their evolution during transport is still elusive. Using electron microscopy, we analyze morphology and mixing state of individual free tropospheric particles transported over long distances above the Atlantic Ocean to the Pico Mountain Observatory (Azores). We find that 70% of the soot particles are highly compacted, while soot with thinly coated exhibits almost spherical aggregated shape. Discrete dipole approximation simulations show that aggregate compaction results in increase of soot single scattering albedo up to 54%. We calculate the top of the atmosphere direct radiative forcing and find it typically smaller for compacted than mass-equivalent fresh soot. The radiative forcing calculated using Mie theory is within 12% of the discrete dipole approximation for compacted particles and high surface albedo; implying that for very aged soot laying above remote marine clouds, Mie calculations might provide a reasonable approximation.

1. Introduction

Soot particles or ns-soot (nanosphere soot) [*Buseck et al.*, 2014], often referred to as black carbon, are aggregates of carbonaceous monomers produced from incomplete combustion of fossil fuel and biomass. Soot particles strongly absorb sun-light, directly impacting Earth's radiation balance [*Bond et al.*, 2013; *Haywood and Ramaswamy*, 1998]. Soot warms the atmospheric layer where it is accumulated, locally strengthening the atmospheric stability. Soot can favor cloud evaporation [*Hansen et al.*, 1997] when it is encapsulated in a cloud droplet, while soot laying above clouds can cause cloud thickening [*Wilcox*, 2012]. Furthermore, soot can facilitate atmospheric heterogeneous reactions due to its large surface area [*Nyeki and Colbeck*, 2000; *Zhang et al.*, 2008], and it can affect climate indirectly by acting as cloud condensation nuclei (CCN) and ice nuclei [*Bond et al.*, 2013; *Tritscher et al.*, 2011; *Zhang et al.*, 2008].

Soot can be transported over long distances and reach remote regions, such as the Arctic or the Himalaya. Soot deposited by wet or dry deposition on snow reduces its albedo and contributes to regional snow melt and global warming [*Hansen and Nazarenko*, 2004; *Ramanathan and Carmichael*, 2008; *Rosen et al.*, 1981]. Uncertainties in the atmospheric radiative forcing of soot are large [*Bond et al.*, 2013]; part of the uncertainties is due to the simplified representation of soot morphology and mixing state in climate models, typically limited to spherical symmetry (homogeneous sphere or at best, core shell configuration) [*Adachi and Buseck*, 2013].

Freshly emitted soot particles are typically hydrophobic, open fractal-like aggregates. During transport, soot undergoes various aging processes such as coagulation, condensation and heterogeneous reactions, resulting in changes in morphology (size, shape and internal structure) and mixing state (soot coating). In a recent laboratory study, *Zangmeister et al.* [2014] show that soot compaction is remarkably independent of the monomer or particle size. The complex

morphology and mixing state of soot significantly impact its aging time scale, as well as, atmospheric life time, affecting its global burden [*Van Poppel et al.*, 2005].

Morphology and mixing state affect soot light scattering and absorption cross sections [*Cross et al.*, 2010; *Khalizov et al.*, 2009; *Lack et al.*, 2012; *Zhang et al.*, 2008], and therefore soot's role on radiative forcing [*Adachi et al.*, 2010; *Van Poppel et al.*, 2005]. Scattering and absorption cross sections of soot change upon compaction depending on the refractive index, the monomer diameter and the structural details [*Liu et al.*, 2008; *Scarnato et al.*, 2013]. Conversely, coatings on soot particles typically enhance both scattering and absorption cross sections, but the magnitude of the enhancement depends on the details of the geometric distribution of the components within each particle [*Adachi and Buseck*, 2013; *Cheng et al.*, 2014].

In this study, we investigate morphology and mixing state of soot particles collected at Pico Mountain Observatory (PMO), Azores, during two long-range transport events in July 2012 in the free-troposphere of the North Atlantic Ocean. The first event with recirculation over the ocean, and the second event with transport from North America. We use scanning electron microscopy (SEM) to characterize the morphology and mixing of soot. We find evidence of extreme soot compaction, and assess its implications on the soot optical properties using discrete dipole approximation (DDA) and Mie simulations. Furthermore, we assess the variations of the direct radiative forcing at the top of the atmosphere (TOA-DRF) due to different degrees of compaction.

2. Experimental methods

2.1 Sampling site and measurements

The PMO site is located in the summit caldera of the Pico Volcano (at 2225m asl, 38.47°N, 28.40°W) in the Azores, Portugal. The mountaintop station (supporting information (SI), Figure

S1) is typically above the marine boundary layer [*Honrath et al.*, 2004; *Kleissl et al.*, 2007; *Rémillard et al.*, 2012]. The station often receives air masses from North America and sometimes from Africa and Europe and is an ideal site to study free-tropospheric aerosol transported over long distances across the Atlantic Ocean [*Dzepina et al.*, 2014].

We investigate two specific events, one on July 06 - 07, 2012 (event-1) and one on July 20 - 21, 2012 (event-2). We perform a retroplume analysis using the Lagrangian particle dispersion model FLEXPART [*Owen and Honrath*, 2009; *Stohl et al.*, 2005], to study the origin of air masses and trajectory to PMO. For event-1, air masses were mostly transported from the south-west Atlantic (Figure 1), while during event-2, air masses were mostly transported from North America. The plume age for event-1 is higher (~15.7 days) than for event-2 (~9.5 days), therefore soot in event-1 was probably more aged.

Particles were collected on nuclepore filters [*China et al.*, 2013], and experimental details are provided in the SI. Individual particle morphology and mixing state are studied using projected images from a field emission SEM (Hitachi S-4700) coupled with an energy dispersive X-ray spectrometer (EDS).

2.2 Particle classification and soot mixing state

Soot particles are identified from their unique aggregate nature, as they are made of carbonaceous spherical monomers (Figure S2). In this classification, "soot" includes soot particles that are mixed within, or coated by other material. We note that SEM analysis is performed in vacuum conditions and provides only surface information (see SI for more detail); these caveats might skew the number of soot particles toward larger fractions than actually present in the atmosphere.

The second step is to visually examine the mixing state of soot. Soot is categorized into four groups: 1) embedded [*Adachi and Buseck*, 2008], where soot is fully engulfed in coating material; 2) partly coated, where the coating material fills the soot internal voids; 3) thinly coated, where coating on soot is minimal; 4) inclusions, where only a part of the soot is mixed with other material or is only partially touching another particle (Figure S3). Details of this classification and limitations are discussed elsewhere [*China et al.*, 2013].

2.3 Parameterization of Soot morphology

Soot particles are considered to be fractal-like aggregates as they exhibit self-similar structures over several length scales [*Oh and Sorensen*, 1997] and can be described using a mass fractal dimension (D_f) [*Mandelbrot*, 1982]. For particles with $D_f < 2$, D_f can be calculated from 2D images using the ensemble method [*Oh and Sorensen*, 1997; *Wentzel et al.*, 2003]. However, soot particles collected at PMO are extremely aged and often highly compacted (with expected D_f substantially larger than 2). Therefore, we did not use the ensemble method to estimate the scaling law, we used instead the measurable projected area of the aggregate (A_a) and its maximum length (L_{max}) [*Lee and Kramer*, 2004]:

$$A_a = k_2 (L_{max})^{D_{2f}} \quad (1)$$

Where we assume the logarithm of A_a to be proportional to the logarithm of the particle mass. We underline that the power law exponent, D_{2f} represents a 2D estimate of the fractal dimension that should be proportional, but not equal to D_f. We applied the above power relation using ensembles of soot particles to provide a measure of the fractal morphology of compacted soot, inclusive of eventual coating material filling voids between monomers.

The size of each particle estimated from 2D SEM images is expressed in terms of projected area equivalent diameter, D_{Aeq}. We use roundness and convexity to further quantify the

compactness of soot. Roundness is the ratio of the projected area of the particle to the area of a circle of diameter equal to L_{max}. Convexity, or solidity, is the ratio of the projected area of the particle to the area of the convex hull polygon (smallest convex polygon that fully covers the particle's projected area) and is a measure of the topological properties of the particle's projection. Details on image processing and morphological parameters are described elsewhere [*China et al.*, 2014].

2.4 Modeling of soot optical properties with different compaction

We model climate relevant optical properties of synthetic soot particles, generated by a random walk aggregation algorithm [*Richard et al.*, 2011], that closely mimic the characteristics of aerosols sampled at PMO. We generate synthetic soot aggregates with an average monomer diameter of 34 nm, and monomer numbers (N) of 66 and 150 (obtained considering the range of monomer overlaps found in this study from thinly coated particles, see SI) and, further, N of 247 considering a constant packing density of 0.36 for compacted soot [*Radney et al.*, 2014; *Zangmeister et al.*, 2014], in agreement with the analysis of PMO samples. Further, we generate the synthetic soot aggregate with different levels of compaction: 1) open chain-like (D_f = 1.8), 2) medium compaction ($2 < D_f < 2.4$), and 3) high compaction ($D_f > 2.67$), in order to represent respectively fresh, medium aged and very aged soot (Table S1).

The optical properties of observationally constrained synthetic particles are calculated using the Discrete Dipole Approximation (DDA-DDSCAT7.3 code) [*Draine and Flatau*, 1994; 2013]. A detailed description of the methods for the aggregate generation and DDA simulations is provided elsewhere [*Scarnato et al.*, 2013]. For the DDA calculations we use a wavelength-dependent refractive index for soot [*Chang and Charalampopoulos*, 1990]. We compute and discuss climate relevant optical properties at 10 wavelengths ranging from 370 nm to 950 nm. The

wavelengths have been selected according to channels used by several remote sensing and in-situ instruments. The optical properties are averages over 1000 random synthetic particle orientations, sufficient to obtain DDA solution convergence for soot aggregates [*Scarnato et al.*, 2013].

We investigate numerically the spectral sensitivity of the scattering (C_{sca}) and absorption (C_{abs}) cross sections, the single scattering albedo (SSA), and the asymmetry parameter (g) to the compactness of bare/uncoated soot, neglecting the effect of coating. For comparison, soot optical properties of mass-equivalent diameter particles are also modeled using Mie theory [*Mätzler*, 2002].

3. Results and Discussion

3.1 Mixing states of soot particles

We analyze a total of 1,317 particles for event-1 and 806 for event-2. The relative abundance of soot particles in event-2, is almost double (~54%) than in event-1 (27%). Soot particles at PMO are typically very compact (Figure 2a-d), while open chain-like soot aggregates are rarely observed during both events.

Freshly emitted soot is typically bare or very thinly coated with an open chain-like structure [*Adachi et al.*, 2007; *China et al.*, 2014; *Wentzel et al.*, 2003]. During atmospheric processing, soot mixes with other compounds or other particles, resulting in different mixing configurations and sometimes in soot restructuring. Figure 2e shows the fraction of different soot mixing categories. The higher fraction of embedded and partly coated soot (87%) in event-2 compared to event-1 (57%) and the higher fraction of thinly coated soot in event-1 (37%) compared to event-2 (9%) suggest different atmospheric processing. Condensation of coating material might be prominent on the less aged soot, during event-2. However, it is also possible that the mixing material in the two events had different volatilities. The finding that the fraction of soot inclusions is small for both events (< 7%) suggests that coagulation processes are possibly less significant, compared to

condensation processes, during long-range transport over the Ocean. In addition, semi-quantitative EDS analysis shows that the elemental composition of embedded particles is mostly dominated by C and O with only a minor fraction of S, suggesting that the embedded material is likely organic. However, for both events, the relative abundance of S for the particles attached to the soot in the soot inclusions category, is higher compared to the S abundance in embedded particles (Table S2). Similarly, a previous study found that 10 – 45% of sulfate particles contained soot as inclusions in clean air above the remote Southern Ocean near Tasmania [*Pósfai et al.*, 1999].

3.2 Morphology of soot particles

Fractal dimension of soot reflects its aging and is affected by a combination of factors, including emission sources, emission conditions, and atmospheric processing pathways [*Adachi et al.*, 2007; *Chakrabarty et al.*, 2014]. Compact soot particles have higher D_f than chain-like open aggregates [*Liu et al.*, 2008]. For example, soot aggregates in Figure 1b and 1c should have a 3-D D_f close to 3 or a 2-D fractal dimension D_{2f} close to 2. On average, D_{2f} estimated from equation (1) is higher for event-2 (1.89 ± 0.02) than event-1 (1.82 ± 0.02) (Figure S6). Higher D_{2f} reflects higher coating or higher compactness. In Table 1 we report the values of D_{2f} for three classes of soot particles.

Embedded soot particles for event-1 have the largest average D_{Aeq}, followed by partly coated and thinly coated soot, suggesting the size of the particle increases as coating increases (Table 1). In contrast, for event-2, the difference in the sizes of embedded and thinly coated soot is small, suggesting that the soot core inside the embedded particle might be smaller in size or that the coating is thinner than for the particles in event-1. The details of the size distributions for the different soot types are discussed in the SI (Figure S4). Note that thinly coated soot have often a very compact morphology, where the aggregate is collapsed in a quasi-spherical shape,

characterized by little void space between the aggregate monomers. The collapse of soot aggregate core leads to a reduction of its surface area compared to freshly emitted soot. Figures 2f-g show the distribution of convexity (roundness, Figure S5) for thinly, partly coated and embedded soot. For both events, the thinly coated soot is very compact (convexity = 0.82) compared to freshly emitted soot collected, for example, near freeway onramps (convexity = 0.69) [*China et al.*, 2014]. However in general, the observed soot is more compact in event-1 than event-2, possibly due to the fact that particles during event-1 might have been more aged and processed.

A recent laboratory study showed that partially aged soot adsorb water upon humidification and turn into efficient CCN, leading to additional soot compaction [*Khalizov et al.*, 2013]. Therefore, cloud or water processing might be responsible for the compacted shape of thinly coated soot that are abundant at PMO. Several previous laboratory studies reported collapsing of soot under the influence of water [*Lewis et al.*, 2009; *Mikhailov et al.*, 1999; *Radney et al.*, 2014; *Weingartner et al.*, 1995; *Zangmeister et al.*, 2014]. It has been hypothesized that capillary forces induced during condensation or filling of soot cavities with water might be responsible for the soot restructuring [*Tritscher et al.*, 2011]. However, others argue that capillary forces during evaporation, instead of condenstation, drive the restructuring of soot by water [*Ebert et al.*, 2002; *Ma et al.*, 2013].

3.3 Optical properties of soot particles

We assess the sensitivity of soot optical properties to compaction by performing DDA simulations. The top panels in Figure 3 illustrate C_{abs} and C_{sca} cross sections, *SSA* and *g* normalized by the corresponding values obtained for fresh soot. Simulations are shown for three different cases of number of monomers (N = 66, 150 and 247). We find a wavelength dependency in the

235 C_{abs} ratio ($C_{abs\text{-}very\ aged}/C_{abs\text{-}fresh}$) as a function of compactness. Compacted, aged soot aggregates
236 have slightly higher C_{abs} compared to fresh soot for wavelengths larger than 500 nm, while the
237 opposite is true for shorter wavelengths. A previous T-matrix study [*Liu et al.*, 2008], also found
238 a similar pattern and suggested two possible reasons: 1) as particles become more compact, less
239 absorbing materials are directly exposed to the incident light, resulting in lower C_{abs} [*Scarnato et*
240 *al., 2013*]; 2) C_{abs} increases for compacted particles due to an increased electromagnetic interaction
241 between monomers [*Liu et al.*, 2008]; this second effect seems to be dominant at longer
242 wavelengths.

243 The C_{sca} ratio ($C_{sca\text{-}very\ aged}/C_{sca\text{-}fresh}$) is higher than 1.5 for $N = 66$ and higher than 2 for $N = 150$
244 and $N = 247$ in the visible wavelength range, but the ratio decreases (although always remaining
245 above unity) in the NIR. The C_{sca} ratio is highest (2.66) for $N = 247$ at 660 nm for very aged soot.
246 As the effect of compaction is substantially higher for scattering than for absorption, the SSA
247 becomes higher as the particle becomes more compact. Increases in SSA and extinction have been
248 recently demonstrated in soot generated in the laboratory and compacted through water processing
249 [*Radney et al.*, 2014]. The SSA ratio ($SSA_{very\ aged}/SSA_{fresh}$) decreases as the wavelength increases.
250 The asymmetry parameter *g*, is a function of both particle size and shape [*Kahnert et al.*, 2012; *Liu*
251 *et al.*, 2008].We found that fresh soot with smaller monomer numbers has higher *g* compared to
252 medium and very aged soot. However, *g* exhibits a different behavior for $N = 150$, with medium
253 aged soot having higher *g*, followed by fresh and aged soot. Similarly, *Liu et al.* [2008] found that
254 *g* reaches the highest values for a $D_f \sim 2$ and starts decreasing as the particle becomes more
255 compact. Furthermore, we compute the optical properties of soot with the same mass-equivalent
256 diameter using Mie calculations to investigate how closely they approach the DDA values. SSA

257 estimated from Mie for compacted soot is within ~ 18% of the DDA value for all three cases of N
258 at 550 nm (Figure S7).

259 We estimate the ratio of the top of the atmosphere direct radiative forcing (TOA-DRF) for
260 medium aged and very aged soot with respect to fresh soot. We perform the calculations following
261 the conceptual formulation by *Chylek and Wong* [1995]. As the surface albedo (a) has an important
262 role in determining the TOA-DRF, we perform the calculations for two extreme values: a = 0.06
263 and 0.8 (see SI for details) that might represent a lower limit for the albedo of the ocean and higher
264 limit for cloud albedo, respectively. The bottom panel of Figure 3 shows that the ratio of the TOA-
265 DRF is close to unity or substantially less than unity, depending on aging, number of monomers
266 and surface albedo. This implies that compaction due to aging typically results in a reduction of
267 the soot TOA-DRF for both values of a. TOA-DRF estimated from DDA and Mie simulations
268 differ substantially for fresh and medium aged soot (up to 27% at 370 nm for a=0.8), but differ by
269 12% for the very aged soot (Figure S8).

270 As mentioned earlier, soot particles observed at PMO are likely cloud processed, and this might
271 be the reason for the very compacted shape with minimal coating on the surface of the particle.
272 This also implies that soot might have been incorporated into water droplets during its journey
273 over the Atlantic. A recent T-matrix study [*Mishchenko et al.*, 2014] on soot-water mixtures shows
274 that orientation-averaged C_{abs} strongly depend on soot morphology and the position inside a water
275 droplet. Orientation-averaged C_{abs} of soot-water mixture is higher for open fractal soot than
276 compacted soot and C_{abs} tends to decrease as the soot particle moves from the center of the droplet
277 to the boundary. This implies that the soot morphology might have an important role in the semi-
278 direct effect as well, with soot compaction resulting in a lower in-cloud absorption and therefore
279 lower positive forcing.

4. Conclusions

In this study, we investigated the morphology and mixing state of soot particles sampled during two events of long-range transport in the North Atlantic free troposphere with different aging times. Due to the unique location of PMO, the results from this study provide a more generalized representation of the morphology and mixing state of aged soot particles than typical point measurements. The predominance of compact soot aggregates (~70% of particles with convexity ≥ 0.80) probably caused by cloud processing, suggests that these structures might be very common in the free troposphere in remote marine environments. The quantitative parameters measured were inputs to numerical simulations that further demonstrated that the forcing strongly depend on the soot morphology for a given soot mass. We determined the enhancements of scattering and absorption from the compaction of aged soot, leading to an overall increase in SSA and a reduction of TOA-DRF compared to freshly emitted soot of the same mass.

The results of this study contribute to better understand: 1) how microphysical processes might affect, in different environments, mixing and morphology of soot, 2) how the variation of soot morphology might affect its optical properties, and 3) their impact on the soot radiative forcing. The results of this study have implications on how soot should be represented in particle-resolving mixing state [*Riemer et al.*, 2009] and chemical transport models [*Wang et al.*, 2013] in remote regions of the free troposphere, and how the correct representation of soot morphology might affect the calculation of the soot radiative forcing in regional and global climate models [*Kahnert and Devasthale*, 2011]. These results also suggest that Mie calculations used in global models might provide a reasonable (within 12%) estimate of the TOA-RF for very aged soot particles in remote free tropospheric environments, such as observed at the PMO. Finally, these results call for future

experiments to further constrain the frequency and the degree of soot compaction in remote regions.

Acknowledgments

The data for this paper are available upon request from the authors. This work was funded by the U.S. Department of Energy's Atmospheric System Research (grant #DE-SC0006941) and the National Science foundation (grant #AGS-1110059). S. China and C. Mazzoleni acknowledge a NASA Earth and Space Science Graduate Fellowship (grant #NNX13AN68H). We thank Dr. C. Sorensen for insightful discussions on the fractal dimension. We thank Jesse Nordeng and Kyle Gorkowski for their crucial role in the development of the SEM sampler. We are especially grateful for the pioneering work of the late Dr. Richard Honrath in establishing the PMO site.

References

Adachi, and P. Buseck (2008), Internally mixed soot, sulfates, and organic matter in aerosol particles from Mexico City, *Atmos. Chem. Phys*, *8*(21), 6469-6481.

Adachi, S. H. Chung, H. Friedrich, and P. R. Buseck (2007), Fractal parameters of individual soot particles determined using electron tomography: Implications for optical properties, *J. Geophys. Res.*, *112*(D14), doi: 10.1029/2006JD008296.

Adachi, K., and P. R. Buseck (2013), Changes of ns-soot mixing states and shapes in an urban area during CalNex, *J. Geophys. Res.*, (118), doi: 10.1002/jgrd.50321.

Adachi, K., S. H. Chung, and P. R. Buseck (2010), Shapes of soot aerosol particles and implications for their effects on climate, *J. Geophys. Res.*, *115*(D15), D15206.

Bond, T. C., et al. (2013), Bounding the role of black carbon in the climate system: A scientific assessment, *J. Geophys. Res.*, *118*(11), 5380-5552.

Buseck, P. R., K. Adachi, A. Gelencsér, É. Tompa, and M. Pósfai (2014), ns-Soot: A Material-Based Term for Strongly Light-Absorbing Carbonaceous Particles, *Aerosol Sci.Tech*, 48 (7) 777-788, doi:10.1080/02786826.2014.919374.

329 Chakrabarty, R. K., N. D. Beres, H. Moosmüller, S. China, C. Mazzoleni, M. K. Dubey, L. Liu,
330 and M. I. Mishchenko (2014), Soot superaggregates from flaming wildfires and their direct
331 radiative forcing, *Sci. rep.*, *4*, 5508, doi:10.1038/srep05508.
332 Chang, H., and T. Charalampopoulos (1990), Determination of the wavelength dependence of
333 refractive indices of flame soot, *Proc. R. Soc. Lond., A: Mathematical and Physical Sciences*,
334 *430*(1880), 577-591.
335 Cheng, T., Y. Wu, and H. Chen (2014), Effects of morphology on the radiative properties of
336 internally mixed light absorbing carbon aerosols with different aging status, *Opt. Express*,
337 *22*(13), 15904-15917.
338 China, S., N. Salvadori, and C. Mazzoleni (2014), Effect of Traffic and Driving Characteristics on
339 Morphology of Atmospheric Soot Particles at Freeway On-Ramps, *Environ. Sci. Technol.*,
340 *48*(6), 3128-3135.
341 China, S., C. Mazzoleni, K. Gorkowski, A. C. Aiken, and M. K. Dubey (2013), Morphology and
342 mixing state of individual freshly emitted wildfire carbonaceous particles, *Nat. Commun*.
343 4:2122, doi: 10.1038/ncomms3122.
344 Chylek, P., and J. Wong (1995), Effect of absorbing aerosols on global radiation budget, *Geophy.*
345 *Res. Lett.*, *22*(8), 929-931.
346 Cross, E. S., T. B. Onasch, A. Ahern, W. Wrobel, J. G. Slowik, J. Olfert, D. A. Lack, P. Massoli,
347 C. D. Cappa, and J. P. Schwarz (2010), Soot particle studies—instrument inter-comparison—
348 project overview, *Aerosol Sci. Tech.*, *44*(8), 592-611.
349 Draine, B. T., and P. J. Flatau (1994), Discrete-dipole approximation for scattering calculations,
350 *JOSA A*, *11*(4), 1491-1499.
351 Draine, B. T., and P. J. Flatau (2013), User guide for the discrete dipole approximation code
352 DDSCAT 7.3, *arXiv preprint arXiv:1305.6497*.
353 Dzepina, K., et al. (2014), Molecular characterization of free tropospheric aerosol collected at the
354 Pico Mountain Observatory: a case study with long range transported biomass burning
355 plumes, *Atmos. Chem. Phys. Discuss.*, *14*(17), 24753-24810.
356 Ebert, M., M. Inerle-Hof, and S. Weinbruch (2002), Environmental scanning electron microscopy
357 as a new technique to determine the hygroscopic behaviour of individual aerosol particles,
358 *Atmos. Environ.*, *36*(39), 5909-5916.

359 Hansen, J., and L. Nazarenko (2004), Soot climate forcing via snow and ice albedos, *Proc. Natl.*
360 *Acad. Sci.USA*, *101*(2), 423-428.
361 Hansen, J., M. Sato, and R. Ruedy (1997), Radiative forcing and climate response, *J. Geophys.*
362 *Res.*, *(1984–2012)*, *102*(D6), 6831-6864.
363 Haywood, J. M., and V. Ramaswamy (1998), Global sensitivity studies of the direct radiative
364 forcing due to anthropogenic sulfate and black carbon aerosols, *J. Geophys. Res.*, *103*(D6),
365 6043-6058.
366 Honrath, R., R. C. Owen, M. Val Martin, J. Reid, K. Lapina, P. Fialho, M. P. Dziobak, J. Kleissl,
367 and D. Westphal (2004), Regional and hemispheric impacts of anthropogenic and biomass
368 burning emissions on summertime CO and O3 in the North Atlantic lower free troposphere,
369 *J. Geophys. Res.*, *(1984–2012)*, *109*(D24).
370 Kahnert, M., and A. Devasthale (2011), Black carbon fractal morphology and short-wave radiative
371 impact: a modelling study, *Atmos. Chem. Phys.*, *11*(22), 11745-11759.
372 Kahnert, M., T. Nousiainen, H. Lindqvist, and M. Ebert (2012), Optical properties of light
373 absorbing carbon aggregates mixed with sulfate: assessment of different model geometries
374 for climate forcing calculations, *Opt. Express*, *20*(9), 10042-10058.
375 Khalizov, A. F., R. Zhang, D. Zhang, H. Xue, J. Pagels, and P. H. McMurry (2009), Formation of
376 highly hygroscopic soot aerosols upon internal mixing with sulfuric acid vapor, *J. Geophys.*
377 *Res.*, *(1984–2012)*, *114*(D5).
378 Khalizov, A. F., Y. Lin, C. Qiu, S. Guo, D. Collins, and R. Zhang (2013), Role of OH-initiated
379 oxidation of isoprene in aging of combustion soot, *Environ. Sci. Technol.*, *47*(5), 2254-2263.
380 Kleissl, J., R. E. Honrath, M. P. Dziobak, D. Tanner, M. Val Martín, R. Owen, and D. Helmig
381 (2007), Occurrence of upslope flows at the Pico mountaintop observatory: A case study of
382 orographic flows on a small, volcanic island, *J. Geophys. Res.*, *(1984–2012)*, *112*(D10).
383 Lack, D. A., J. M. Langridge, R. Bahreini, C. D. Cappa, A. M. Middlebrook, and J. P. Schwarz
384 (2012), Brown carbon and internal mixing in biomass burning particles, *Proc. Natl. Acad.*
385 *Sci.*, 109 (37), 14,802-14,807.
386 Lee, C., and T. A. Kramer (2004), Prediction of three-dimensional fractal dimensions using the
387 two-dimensional properties of fractal aggregates, *Adv. Colloid Interface Sci.*, *112*(1-3), 49-
388 57.

389 Lewis, K., W. Arnott, H. Moosmüller, R. Chakrabarty, C. Carrico, S. Kreidenweis, D. Day, W.
390 Malm, A. Laskin, and J. Jimenez (2009), Reduction in biomass burning aerosol light
391 absorption upon humidification: roles of inorganically-induced hygroscopicity, particle
392 collapse, and photoacoustic heat and mass transfer, *Atmos. Chem. Phys*, *9*(22), 8949-8966.
393 Liu, M. I. Mishchenko, and W. P. Arnott (2008), A study of radiative properties of fractal soot
394 aggregates using the superposition T-matrix method, *J. Quant. Spectrosc. Ra*, *109*(15), 2656-
395 2663.
396 Ma, X., C. D. Zangmeister, J. Gigault, G. W. Mulholland, and M. R. Zachariah (2013), Soot
397 aggregate restructuring during water processing, *Journal of Aerosol Science*, *66*(0), 209-219.
398 Mandelbrot, B. B. (1982), *The Fractal Geometry of Nature*, W.H. Freeman, San Francisco.
399 Mätzler, C. (2002), MATLAB functions for Mie scattering and absorption, version 2, *IAP Res.*
400 *Rep*, *8*.
401 Mikhailov, E., S. Vlasenko, L. Kramer, and R. Niessner (1999), Soot particle restructuring due to
402 interaction with water droplets, *Journal of Aerosol Science*, *30*.
403 Mishchenko, M. I., L. Liu, B. Cairns, and D. W. Mackowski (2014), Optics of water cloud droplets
404 mixed with black-carbon aerosols, *Opt. Lett.*, *39*(9), 2607-2610.
405 Nyeki, S., and I. Colbeck (2000), The Influence of Morphological Restructuring of Carbonaceous
406 Aerosol on Microphysical Atmospheric Processes, in *Aerosol Chemical Processes in the*
407 *Environment*, edited by K. R. Spurny, CRC Press.
408 Oh, C., and C. M. Sorensen (1997), The effect of overlap between monomers on the determination
409 of fractal cluster morphology, *J. Colloid Interf. Sci.*, *193*(1), 17-25.
410 Owen, R. C., and R. E. Honrath (2009), Technical note: a new method for the Lagrangian tracking
411 of pollution plumes from source to receptor using gridded model output, *Atmos. Chem. Phys.*,
412 *9*(7), 2577-2595.
413 Pósfai, M., J. R. Anderson, P. R. Buseck, and H. Sievering (1999), Soot and sulfate aerosol
414 particles in the remote marine troposphere, *J. Geophys. Res.*, *(1984–2012)*, *104*(D17), 21685-
415 21693.
416 Radney, J. G., R. You, X. Ma, J. M. Conny, M. R. Zachariah, J. T. Hodges, and C. D. Zangmeister
417 (2014), Dependence of Soot Optical Properties on Particle Morphology: Measurements and
418 Model Comparisons, *Environ. Sci. Technol.*, *48*(6), 3169-3176.

419 Ramanathan, V., and G. Carmichael (2008), Global and regional climate changes due to black
420 carbon, *Nature Geoscience*, *1*(4), 221-227.
421 Rémillard, J., P. Kollias, E. Luke, and R. Wood (2012), Marine Boundary Layer Cloud
422 Observations in the Azores, *J. Climate*, *25*(21).
423 Richard, D., D. Glenar, T. Stubbs, S. Davis, and A. Colaprete (2011), Light scattering by complex
424 particles in the Moon's exosphere: Toward a taxonomy of models for the realistic simulation
425 of the scattering behavior of lunar dust, *Planetary and Space Science*, *59*(14), 1804-1814.
426 Riemer, N., M. West, R. A. Zaveri, and R. C. Easter (2009), Simulating the evolution of soot
427 mixing state with a particle-resolved aerosol model, *J. Geophys. Res.*, *114*.
428 Rosen, H., T. Novakov, and B. Bodhaine (1981), Soot in the Arctic, *Atmos. Environ. (1967)*, *15*(8),
429 1371-1374.
430 Scarnato, B. V., S. Vahidinia, D. T. Richard, and T. W. Kirchstetter (2013), Effects of internal
431 mixing and aggregate morphology on optical properties of black carbon using a discrete
432 dipole approximation model, *Atmos. Chem. Phys.*, *13*(10), 5089-5101.
433 Stohl, A., C. Forster, A. Frank, P. Seibert, and G. Wotawa (2005), Technical note: The Lagrangian
434 particle dispersion model FLEXPART version 6.2, *Atmos. Chem. Phys.*, *5*(9), 2461-2474.
435 Tritscher, T., Z. Jurányi, M. Martin, R. Chirico, M. Gysel, M. F. Heringa, P. F. DeCarlo, B. Sierau,
436 A. S. Prévôt, and E. Weingartner (2011), Changes of hygroscopicity and morphology during
437 ageing of diesel soot, *Environ. Res. Lett.*, *6*(3), 034026.
438 Van Poppel, L. H., H. Friedrich, J. Spinsby, S. H. Chung, J. H. Seinfeld, and P. R. Buseck (2005),
439 Electron tomography of nanoparticle clusters: Implications for atmospheric lifetimes and
440 radiative forcing of soot, *Geophy. Res. Lett.*, *32*(24).
441 Wang, H., R. C. Easter, P. J. Rasch, M. Wang, X. Liu, S. J. Ghan, Y. Qian, J. H. Yoon, P. L. Ma,
442 and V. Vinoj (2013), Sensitivity of remote aerosol distributions to representation of cloud–
443 aerosol interactions in a global climate model, *Geosci. Model Dev.*, *6*(3), 765-782.
444 Weingartner, E., U. Baltensperger, and H. Burtscher (1995), Growth and structural change of
445 combustion aerosols at high relative humidity, *Environ. Sci. Technol.*, *29*(12), 2982-2986.
446 Wentzel, M., H. Gorzawski, K. H. Naumann, H. Saathoff, and S. Weinbruch (2003), Transmission
447 electron microscopical and aerosol dynamical characterization of soot aerosols, *J. Aerosol*
448 *Sci.*, *34*(10), 1347-1370.

Wilcox, E. (2012), Direct and semi-direct radiative forcing of smoke aerosols over clouds, *Atmos. Chem. Phys.*, *12*(1), 139-149.

Zangmeister, C. D., J. G. Radney, L. T. Dockery, J. T. Young, X. Ma, R. You, and M. R. Zachariah (2014), Packing density of rigid aggregates is independent of scale, *Proc. Natl. Acad. Sci.*, *111*(25), 9037-9041.

Zhang, R., A. F. Khalizov, J. Pagels, D. Zhang, H. Xue, and P. H. McMurry (2008), Variability in morphology, hygroscopicity, and optical properties of soot aerosols during atmospheric processing, *Proc. Natl. Acad. Sci. 105*(30), 10291-10296.

Table 1: Morphological parameters of thinly coated, partly coated and embedded soot particles.

	n		D_{Aeq} (nm)		*Convexity*		*RN*		D_{2f}		k_2	
	E-1	E-2	E-1	E-2	E-1	E-2	E-1	E-2	E-1	E-2	E-1	E-2
Thinly coated	153	36	249 (8)	245 (20)	0.85 (0.01)	0.79 (0.01)	0.60 (0.01)	0.50 (0.02)	1.81 (0.04)	1.85 (0.08)	0.37 (0.02)	0.32 (0.04)
Partly coated	189	230	262 (9)	206 (7)	0.84 (0.01)	0.82 (0.01)	0.57 (0.01)	0.55 (0.01)	1.81 (0.03)	1.88 (0.03)	0.35 (0.02)	0.36 (0.02)
Embedded	46	122	283 (13)	236 (12)	0.88 (0.01)	0.85 (0.01)	0.61 (0.01)	0.57 (0.01)	1.84 (0.07)	1.90 (0.04)	0.40 (0.03)	0.39 (0.02)

Number of particles analyzed (*n*), area equivalent diameter (D_{Aeq}), convexity, roundness (*RN*), power law exponent, or 2D fractal dimension (D_{2f}) and 2D prefactor (k_2). E-1 represents event-1 and E-2 represents event-2. In parenthesis: standard errors for D_{2f} and k_2 calculated from the uncertainty in the least-squares fit, and standard errors for the other parameters.

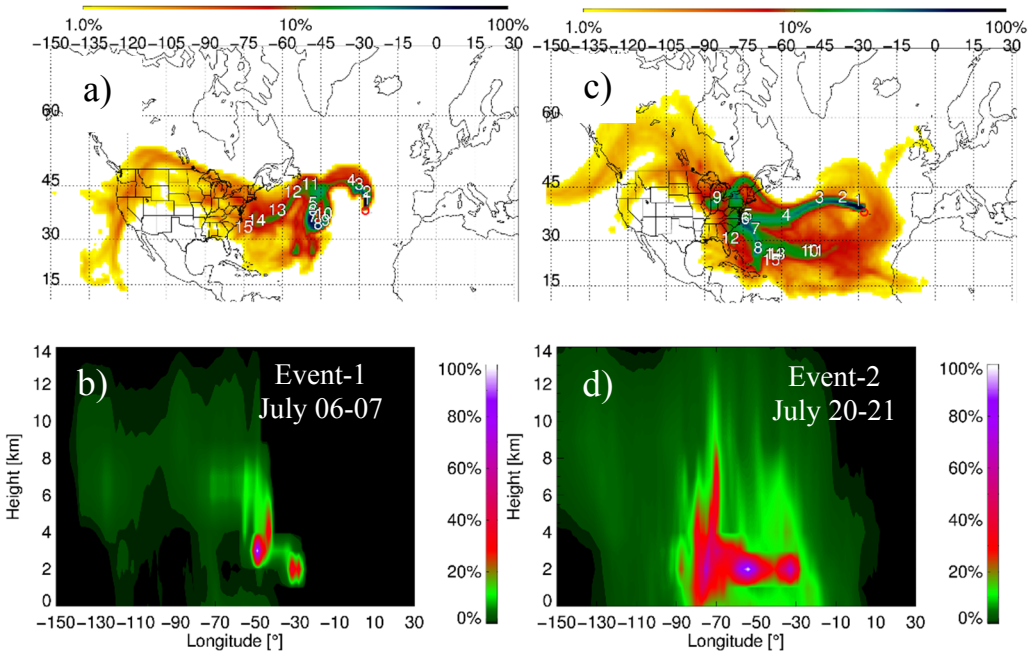

Figure 1: FLEXPART retroplumes show the transport pattern for event-1 (left panel) and for event-2 (right panel). Top panels (a and c) show the column-integrated horizontal transport from all height levels while bottom panels (b and d) show the vertical distribution. The logarithmic color grades indicate the ratio of residence time at each pix to the highest residence time on the panel.

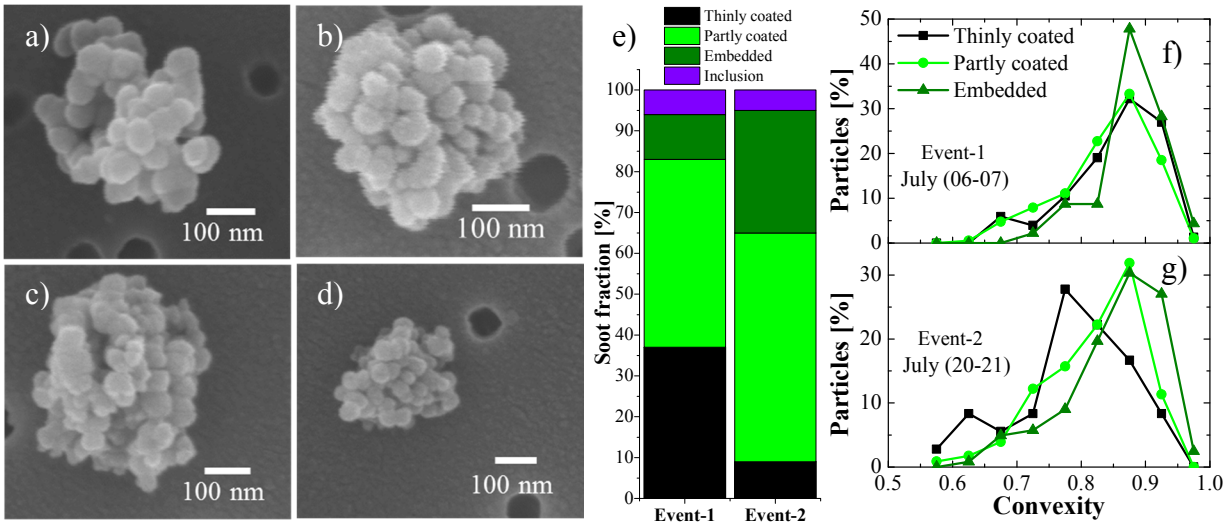

Figure 2: Left SEM images (a-d) show typical morphologies of soot observed at PMO. Middle panel (e) shows the fraction of thinly coated, partly coated, embedded and inclusion soot for event-1 and event-2. Right panels (f-g) show convexity distribution for thinly coated (black), partly coated (light green) and embedded (olive green) soot for event-1 and event-2.

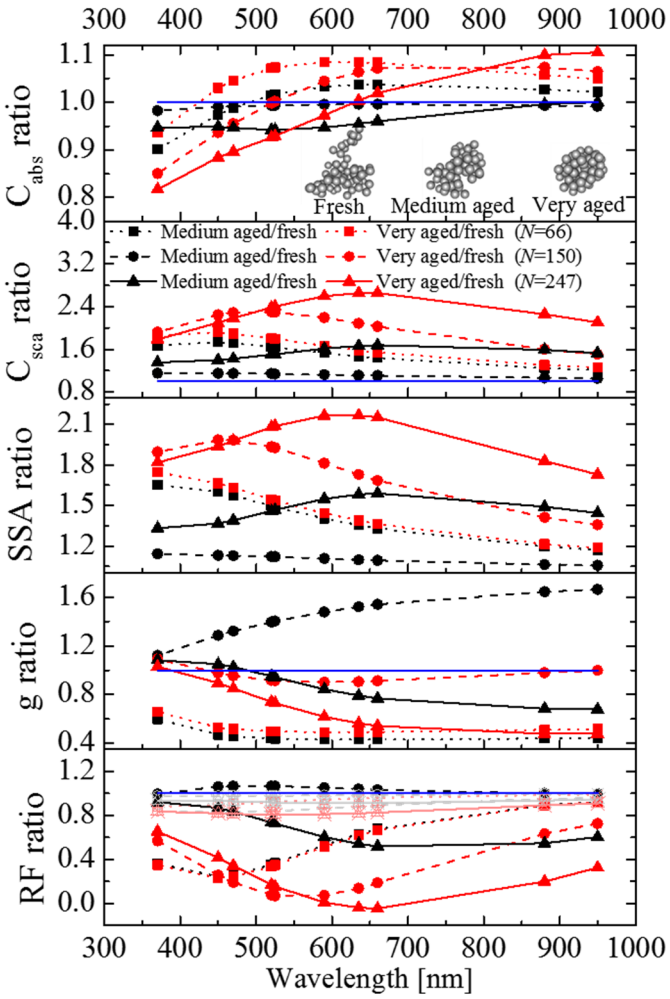

Figure 3: Normalized (ratio) absorption and scattering cross-sections, single scattering albedo (SSA), asymmetry parameter (g), and top of the atmosphere direct radiative forcing (RF) as functions of wavelength for three cases of number of monomers (N=66, square; N=150, round; N=247, triangle points). The blue solid line represents a ratio of one. We use the cross sections, SSA and g of fresh soot as normalizing values. The inset shows the morphology of the synthetic soot used in the simulations for one of the number of monomers (N=66) cases. The synthetic particles represent fresh, medium-aged, and very-aged soot from left to right. RF ratios for low surface albedo (a = 0.06) are represented in black and red, and for high surface albedo (a = 0.8) in gray and light red.